Table-top high-energy 7 μm OPCPA and 260 mJ Ho:YLF pump laser

U. Elu, T. Steinle, D. Sanchez, L. Maidment, K. Zawilski, P. Schunemann, U. Zeitner, C. Simon-Boisson, J. Biegert

Optics Letters

Table-top high-energy 7 μm OPCPA and 260 mJ Ho:YLF pump laser

U. Elu,[1,*] T. Steinle,[1] D. Sánchez,[1] L. Maidment,[1] K. Zawilski,[2] P. Schunemann,[2] U. D. Zeitner,[3] C. Simon-Boisson,[4] and J. Biegert[1,5]

[1]ICFO—Institut de Ciencies Fotoniques, The Barcelona Institute of Science and Technology, 08860 Castelldefels, Barcelona, Spain
[2]BAE Systems, MER15-1813, P.O. Box 868, Nashua, New Hampshire 03061, USA
[3]Fraunhofer Institute of Applied Optics and Precision Engineering, A.-Einstein-Str. 7, 07745 Jena, Germany
[4]THALES Optronique S.A.S., Laser Solutions Unit, 2 avenue Gay-Lussac, 78995 Elancourt Cedex, France
[5]ICREA, Pg. Lluis Companys 23, 08010 Barcelona, Spain
*Corresponding author: ugaitz.elu@icfo.eu

Received 25 April 2019; revised 27 May 2019; accepted 28 May 2019; posted 31 May 2019 (Doc. ID 365484); published 17 June 2019

We present a state-of-the-art compact high-energy mid-infrared (mid-IR) laser system for TW-level eight-cycle pulses at 7 μm. This system consists of an Er:Tm:Ho:fiber MOPA which serves as the seeder for a ZGP-based optical parametric chirped pulse amplification (OPCPA) chain, in addition to a Ho:YLF amplifier which is Tm:fiber pumped. Featuring all-optical synchronization, the system delivers 260 mJ pump energy at 2052 nm and 16 ps duration at 100 Hz with a stability of 0.8% rms over 20 min. We show that chirp inversion in the OPCPA chain leads to excellent energy extraction and aids in compression of the 7 μm pulses to eight optical cycles (188 fs) in bulk BaF_2 with 93.5% efficiency. Using 21.7 mJ of the available pump energy, we generate 0.75 mJ energy pulses at 7 μm due to increased efficiency with a chirp inversion scheme. The pulse quality of the system's output is shown by generating high harmonics in ZnSe which span up to harmonic order 13 with excellent contrast. The combination of the passive carrier-envelope phase stable mid-IR seed pulses and the high-energy 2052 nm picosecond pulses makes this compact system a key enabling tool for the next generation of studies on extreme photonics, strong field physics, and table-top coherent X-ray science.

https://doi.org/10.1364/OL.44.003194

Ultrafast and intense ($> 10^{14}$ W/cm^2) pulses with carrier-to-envelope-phase (CEP) stability give rise to extreme photonic applications such as strong field ionization [1,2], or the generation of isolated attosecond pulses in the extreme ultraviolet range [3,4]. High-energy mid-infrared (mid-IR) pulses through ponderomotive energy scaling provide unique capabilities for the generation of soft x-ray harmonics up to the kilo electron volt level [5–10]. Intense mid-IR pulses can be generated from compact table-top systems, providing an exciting approach towards a new generation of miniature particle accelerators though wakefield acceleration [11]. Low atmospheric losses at wavelengths between 8 and 14 μm provide an opportunity to exploit self-guided pulses via filamentation over kilometer distances without losing intensity through absorption or diffraction [1]. Thus, there is an important demand on high-energy mid-IR pulses which provide CEP-controlled electric field waveforms.

The challenge of generating broadband mid-IR pulses has been approached by direct laser generation, as well as difference frequency generation (DFG) or optical parametric amplification. Solid-state lasers based on Cr:ZnSe and Cr:ZnS have been demonstrated producing nanojoule-level short pulses in the 2–3 μm spectral range [12,13], but amplification to the millijoue level has not been realized, and no realistic materials exist to directly operate in a mode-locked mode at mid-IR wavelengths. DFG has been studied exploiting different nonlinear crystals such as CSP, GaSe, and OPGaP [14–16]. All of these crystals show low-absorption coefficients in the mid-IR, as well as in the near-infrared (NIR) regime, making them suitable to seed the DFG process with commercial NIR fiber lasers for the generation of mid-IR pulses. Unfortunately, the generated mid-IR pulse energy is typically limited to a few pico-joules, mainly due to the low damage threshold of these mid-IR crystals and the high multi-photon absorption coefficients [17,18]. Recent intrapulse DFG experiments [19] have generated broad mid-IR spectra with nanojoule-level pulse energy [20,21] which are very promising for spectroscopy applications [22,23], but do not reach ultra-intense levels.

Therefore, efficient energy scaling systems with suitable mid-IR nonlinear crystals are required to increase the energy to the millijoule level. Optical parametric chirped pulse amplification (OPCPA) can address this problem [24,25], though it has been recognized that in order to amplify wavelengths beyond 5 μm a new pump platform had to be developed to optimize the quantum efficiency [26,27] and mitigate crystal defect-related damages [28]. Previously, we have demonstrated the first compact 7 μm millijoule level platform based on a Ho:YLF based chirped pulse amplifier (CPA) at 2 μm as the pump [26] and a ZGP-based OPCPA for the energy scaling

of the mid-IR pulses [24] with all-optical synchronization [29]. However, using a diffraction grating-based pulse compressor in this spectral range at the end of an OPCPA restricts the pulse energy of the compressed output pulses due to the low efficiency of commercially available gratings.

Here we present a new scheme which incorporates a chirp inversion inside the OPCPA chain, thus permitting us to mitigate adverse chirp-related amplification effects and to use bulk material for stretching and compression. While the relative energy loss due to the insertion of the chirp inverter remains equal, placing it earlier in the amplification chain reduces the absolute energy spent for dispersion tailoring and thereby increases the overall system conversion efficiency. Thus, the overall efficiency of the OPCPA after compression could be doubled with the chirp inversion scheme. We have also upgraded the pump laser system from 40 to 260 mJ at a 100 Hz repetition rate, while maintaining the high stability and reliability of the CPA system. The high-energy 2052 nm pump laser is used for amplification of the optically synchronized passively CEP stable 7 μm seed pulses in an OPCPA chain separated by the chirp inverter, analog to the previous demonstration with our 3 μm OPCPA system [30]. We start by discussing the 2052 nm CPA pump laser system and then report on our results in energy scaling and characterization of millijoule-level 7 μm femtosecond pulses.

The conceptual layout of the high-energy Ho:YLF CPA is shown in Fig. 1. Narrowband nanojoule pulses from the Er:fiber laser are temporally stretched to 340 ps by a chirped volume Bragg grating (CVBG), and the repetition rate is reduced to 100 Hz with a Pockels cell (PC) pulse picker. The 100 Hz pulses are then used to seed a regenerative amplifier based on a water-cooled Ho:YLF crystal, which is pumped by 24 W from a CW Tm:fiber laser (IPG Photonics) centered at 1940 nm.

The regenerative amplifier achieves amplification from 2 nJ to 4 mJ pulse energy. Its cavity is operated in saturation ensuring highly stable performance and excellent beam quality, both being crucial for optimum performance of the entire system. Subsequently, the 4 mJ pulses are introduced in a booster multi-pass amplifier for energy scaling purposes. The booster amplifier is based on a loose focusing triple-pass geometry using a 50 mm long Ho:YLF active material which is cryogenically cooled to 95 K. The booster is pumped in a single-pass loose

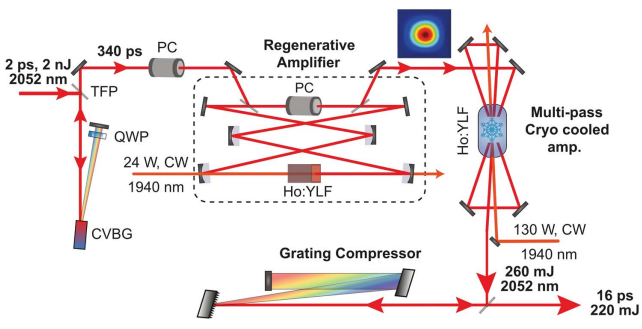

Fig. 1. Layout of the 2052 nm Ho:YLF solid-state laser system. The narrowband 2052 nm pulses from the three-color fiber front-end are stretched in a CVBG, and the repetition rate is reduced in a PC before amplification in a water-cooled regenerative amplifier and cryogenic cooled booster amplifier consecutively. Finally, the stretched pulses are back compressed using a pair of dielectric-coated gratings.

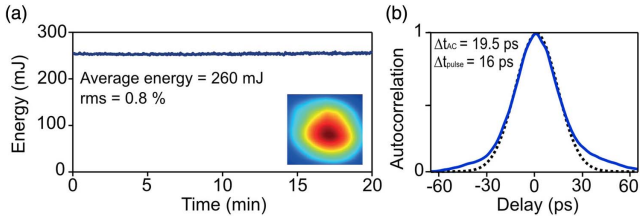

Fig. 2. (a) Measured stability at full power from the Ho:YLF pump system. The inset shows the beam profile measured at full power. (b) Measured intensity autocorrelation (blue) of the 2052 nm pump pulses after compression in the dielectric-coated gratings, together with a Gaussian fit (dashed black). The FWHM duration of the autocorrelation signal was measured to be 19.5 ps corresponding to a pulse duration of 16 ps at FWHM.

focusing geometry using a 120-W CW thulium fiber laser (IPG Photonics) centered at 1940 nm. The booster amplifier increases pulse energy from 4 to 42 mJ in the first pass, to 173 mJ in the second pass, and to 260 mJ in the third pass.

The pulse-to-pulse stability of 0.8% rms over 20 min at 260 mJ (26 W) is shown in Fig. 2(a). Together with excellent beam quality, this makes the system ideal for pumping the mid-IR OPCPA chain.

To temporally compress the high-energy 2052 nm pulses, the beam size is increased to 6 mm (FWHM) to avoid damage to optics. The grating compressor consists of two dielectric-coated gratings (Fraunhofer IOF), with 900 lines/mm and has a footprint of 140 cm by 25 cm. We measure an overall efficiency of 85% corresponding to a final compressed pulse energy of 220 mJ.

Figure 2(b) shows the results from the characterization of the high-energy picosecond pulses via a non-collinear intensity autocorrelation using a 200 μm thick BBO crystal for second-harmonic generation (HHG). The pulse duration, assuming a Gaussian deconvolution is 16 ps; the wings results from uncompensated for higher-order phase. While the 2052 nm spectrum allows pulse compression down to 5 ps, we set the pulse duration to 16 ps in order to maintain a reasonable peak intensity within the limited aperture on the ZGP nonlinear crystals for the OPCPA stages.

Figure 3 shows a schematic of the 7 μm OPCPA system. The two femtosecond outputs from the Er:Tm:Ho:fiber front-end are combined in collinear geometry in a 1 mm thick GaSe nonlinear crystal for type I DFG. Mixing the 1.5 μm, 70 fs, and 2 μm, 100 fs pulses in GaSe, we are able to generate 7 pJ of mid-IR pulses centered at 7 μm.

The 7 μm DFG pulses are stretched in a 16 mm long BaF_2 rod to a pulse duration of 4 ps. All the OPCPA stages are based on non-collinear geometry with an external angle between the pump and seed of 6.5 deg and type I phase-matching configuration in ZGP nonlinear crystals (BAE Systems). The OPCPA consists of two sections, a pre-amplification and a booster amplification section with an intermediate chirp inversion stage. The pre-amplification section is based on two 3 mm thick uncoated ZGP-based OPCPA stages pumped by 200 μJ and 1.5 mJ 2052 nm pulses and achieving 7 μm amplification to 0.1 and 20 μJ, respectively.

The chirp inversion stage between the amplification sections is based on a Martinez-type stretcher which provides control on the stretching factor of the 7 μm pulses, optimizing the

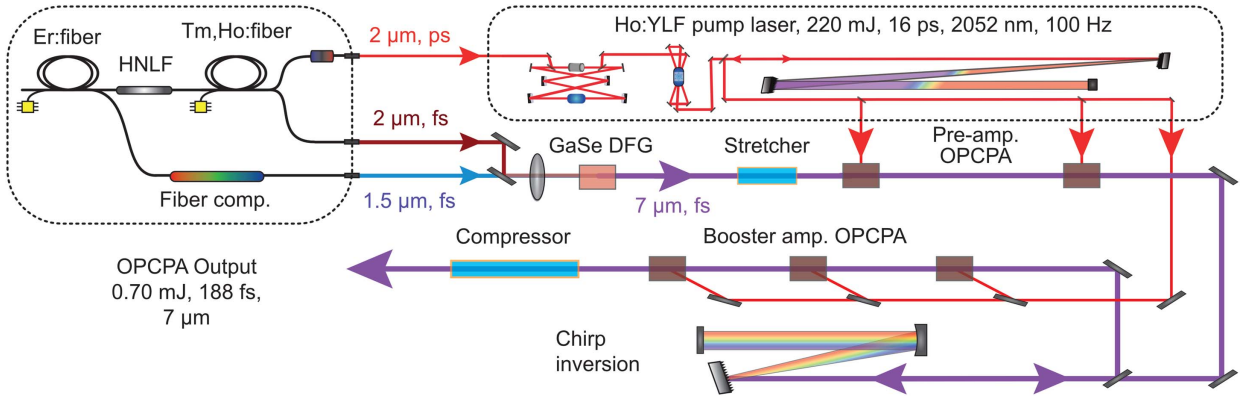

Fig. 3. Layout of the 7 μm OPCPA. The mid-IR seed is generated using the two broadband femtosecond outputs from a three-color fiber front-end via DFG. Afterward, the mid-IR pulses are stretched in a dielectric bulk and consecutively amplified in a pre-amplifier and a booster amplifier separated with a chirp inversion stage. Maximum efficiency of the OPCPA is achieved by tailoring the seed-to-pump pulse durations in the pre-amplifier and booster amplifier. The broadband high-energy mid-IR pulses are recompressed using a dielectric bulk rod of BaF_2.

efficiency of the booster OPCPA stages and allowing the final pulse compression in a bulk dielectric medium. The chirp inverter is aligned to stretch the 7 μm pulses from a negatively chirped 4 ps duration (-1.77×10^5 fs^2) to positively chirped 11 ps pulse duration (5.3×10^5 fs^2) in order to optimize the temporal overlap between mid-IR seed and 2052 nm pump pulses. Moreover, the chirp inverter not only gives us the opportunity to tailor the seed pulse duration, but also ensures an efficient compression scheme in dielectric bulk at the end of the OPCPA. This is important as in the current implementation of the chirp inversion stage exhibits an overall efficiency of 10% due to the limitations imposed by commercially available mid-IR gratings. The chirp inverter was placed in the pre-amplification stages of the OPCPA after reaching an acceptable power level at 7 μm for the alignment of the corresponding optics.

The booster amplifier is based on three consecutive OPCPA stages, with the first stage based on 5 mm thick uncoated ZGP largely to compensate for the losses imparted by the chirp inverter, to restore the pulse energy to 50 μJ. The next and the last stage are composed of two identical 2 mm thick anti-reflection (AR)-coated ZGP crystals and pumped by 3.5 and 15 mJ. This configuration results in amplified pulse energies of 0.25 and 0.75 mJ, respectively. The pump peak intensity in the OPCPA stages was set to be between 2 and 4 GW/cm^2 to avoid damage on the ZGP crystals. The pump energy used in the OPCPA is presently limited to 21.7 mJ due to the aperture size of 8 mm × 8 mm of the ZGP crystals. Due to the challenges associated with proper characterization and propagation of the mid-IR pulses, all the linear and nonlinear processes were numerically pre-simulated using the Simulation System for Optical Science (Sisyfos) nonlinear wave propagation code [31].

The final compression of the mid-IR pulses occurs in a 48 cm long BaF_2 rod that compensates for the dispersion acquired in the chirp inversion stage and shows an overall transmission efficiency of 93.5%, corresponding to a final compressed pulse energy of 0.7 mJ. Characterization of these pulses is done using a home-built all-reflective optics-based third-harmonic generation frequency-resolved optical gating (THG FROG) device using a thin ZnSe crystal for the generation of the third-harmonic. This characterization technique allows us to measure the signal of the FROG using a thermo-electric cooler-based NIR spectrometer without the need for using mid-IR nitrogen cooled detectors or less precise mid-IR photodiodes. Furthermore, the THG FROG has allowed a fast reconstruction of full pulse amplitude and phase of our high-energy mid-IR pulses showing a FWHM pulse duration of the 7 μm pulses of 188 fs, see Fig. 4.

To test the fidelity of the compression we employed the high-energy broadband mid-IR pulses for HHG in a ZnSe sample. Owing to the materials' polycrystalline nature, we observe both even and odd harmonics up to the 13th order (Fig. 5). The high-energy 7 μm pulses are focused in the sample to a spot size of 136 μm at FWHM, which is shown in the inset of Fig. 5, using a 75 mm off-axis parabolic mirror, and the visible and NIR harmonics are then collimated with a $f =$ 75 mm fused silica lens. Using these focusing conditions and employing 50 μJ of 7 μm energy (limited to avoid damage to the ZnSe), we estimate the peak intensity to be 0.45 TW/cm^2. By splitting the NIR and visible spectral parts using a silicon thin plate, we measure all the harmonics below the bandgap simultaneously with integration times lower than 500 ms. The HHG emission is fiber-coupled into the spectrometers using a NIR256 spectrometer (Ocean Optics) for the spectral range of 900–2550 nm and a HR4000 visible spectrometer (Ocean Optics) for the range of 200–1100 nm.

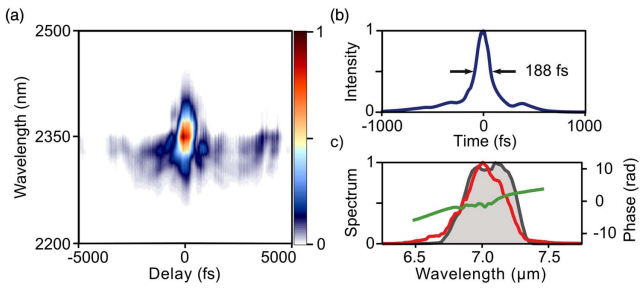

Fig. 4. Pulse characterization of the 7 μm compressed pulses. (a) Measured third-harmonic FROG, (b) the retrieved pulse envelope with 188 fs FWHM duration, and (c) measured (filled gray) and retrieved spectrum (red line) and phase (green line).

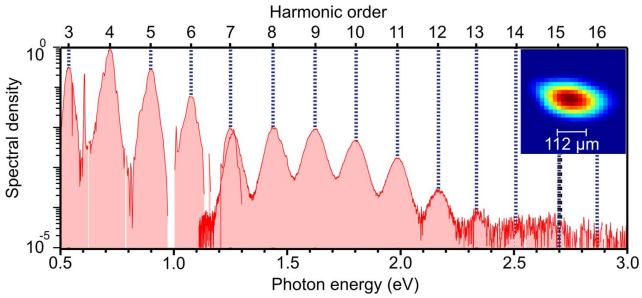

Fig. 5. Measured high-harmonic spectrum in bulk ZnSe crystal (red curve) and the harmonic orders from the third to 13th harmonic, both even and odd, shown in dashed blue lines. The black thick dashed line refers to the bandgap of the crystal. The inset shows the measured beam profile of the 7 µm pulses at the generation plane of the harmonics.

In conclusion, we have demonstrated an all-optically synchronized CPA and OPCPA system generating 260 mJ pulses centered at 2052 nm and 0.75 mJ mid-IR pulses at 7 µm at a 100 Hz repetition rate. We demonstrated that the chirp inversion scheme improved the total OPCPA efficiency and allowed reaching the millijoule-level with a demonstrated pulse energy of 0.7 mJ at 188 fs after compression (eight optical cycles). The quality of the compressed high-energy 7 µm pulses was demonstrated through HHG in ZnSe by achieving a spectrum expanding over all the visible and NIR regime up to order 13. This mid-IR OPCPA platform features the highest demonstrated energies for both 2052 nm and 7 µm pulses and represents a significant step towards mid-IR high-field applications such as coherent kilo electron volt x-rays or self-similar atmospheric propagation and laser-plasma acceleration.

Funding. Ministerio de Economía y Competitividad (MINECO) (FIS2017-89536-P); "Severo Ochoa" Programme for Centres of Excellence in R&D (SEV-2015-0522); FET-OPEN "PETACom" (829153); Agència de Gestió d'Ajuts Universitaris i de Recerca (AGAUR); Fundación Cellex (SGR 1639); Army Research Laboratory (ARL) (W911NF-17-1-0565); H2020 European Research Council (ERC) (788218, 840010); Horizon 2020 Framework Programme (H2020) (654148).

REFERENCES

1. S. Tochitsky, E. Welch, M. Polyanskiy, I. Pogorelsky, P. Panagiotopoulos, M. Kolesik, E. M. Wright, S. W. Koch, J. V. Moloney, J. Pigeon, and C. Joshi, Nat. Photonics **13**, 41 (2019).
2. B. Wolter, M. G. Pullen, M. Baudisch, M. Sclafani, M. Hemmer, A. Senftleben, C. D. Schröter, J. Ullrich, R. Moshammer, and J. Biegert, Phys. Rev. X **5**, 021034 (2015).
3. M. Hentschel, R. Kienberger, C. Spielmann, G. A. Reider, N. Milosevic, T. Brabec, P. Corkum, U. Heinzmann, M. Drescher, and F. Krausz, Nature **414**, 509 (2001).
4. S. M. Teichmann, F. Silva, S. L. Cousin, M. Hemmer, and J. Biegert, Nat. Commun. **7**, 11493 (2016).
5. S. L. Cousin, N. Di Palo, B. Buades, S. M. Teichmann, M. Reduzzi, M. Devetta, A. Kheifets, G. Sansone, and J. Biegert, Phys. Rev. X **7**, 041030 (2017).
6. J. Biegert, P. K. Bates, and O. Chalus, IEEE J. Sel. Top. Quantum Electron. **18**, 531 (2012).
7. J. Tate, T. Auguste, H. G. Muller, P. Salières, P. Agostini, and L. F. DiMauro, Phys. Rev. Lett. **98**, 013901 (2007).
8. T. Popmintchev, M. Chen, O. Cohen, M. Grisham, J. Rocca, M. Murnane, and H. Kapteyn, Opt. Lett. **33**, 2128 (2008).
9. M. V. Frolov, N. L. Manakov, and A. F. Starace, Phys. Rev. Lett. **100**, 173001 (2008).
10. T. Popmintchev, M. C. Chen, D. Popmintchev, P. Arpin, S. Brown, S. Alisauskas, G. Andriukaitis, T. Balciunas, O. D. Mucke, A. Pugzlys, A. Baltuska, B. Shim, S. E. Schrauth, A. Gaeta, C. H. García, L. Plaja, A. Becker, A. Jaron'Becker, M. M. Murnane, and H. C. Kapteyn, Science **336**, 1287 (2012).
11. D. Woodbury, L. Feder, V. Shumakova, C. Gollner, R. Schwartz, B. Miao, F. Salehi, A. Korolov, A. Pugžlys, A. Baltuška, and H. M. Milchberg, Opt. Lett. **43**, 1131 (2018).
12. Y. Wang, T. T. Fernandez, N. Coluccelli, A. Gambetta, P. Laporta, and G. Galzerano, Opt. Express **25**, 25193 (2017).
13. S. Vasilyev, I. Moskalev, V. Smolski, J. Peppers, M. Mirov, V. Fedorov, D. Martyshkin, S. Mirov, and V. Gapontsev, Optica **6**, 126 (2019).
14. S. Chaitanya Kumar, M. Jelínek, M. Baudisch, K. T. Zawilski, P. G. Schunemann, V. Kubeček, J. Biegert, and M. Ebrahim-Zadeh, Opt. Express **20**, 15703 (2012).
15. D. Sánchez, M. Hemmer, M. Baudisch, K. Zawilski, P. Schunemann, H. Hoogland, R. Holzwarth, and J. Biegert, Opt. Lett. **39**, 6883 (2014).
16. H. Timmers, A. Kowligy, A. Lind, F. C. Cruz, N. Nader, M. Silfies, G. Ycas, T. K. Allison, P. G. Schunemann, S. B. Papp, and S. A. Diddams, Optica **5**, 727 (2018).
17. A. Schliesser, N. Picqué, and T. W. Hänsch, Nat. Photonics **6**, 440 (2012).
18. V. Petrov, Opt. Mater. **34**, 536 (2012).
19. I. Pupeza, D. Sánchez, J. Zhang, N. Lilienfein, M. Seidel, N. Karpowicz, T. Paasch-Colberg, I. Znakovskaya, M. Pescher, W. Schweinberger, V. Pervak, E. Fill, O. Pronin, Z. Wei, F. Krausz, A. Apolonski, and J. Biegert, Nat. Photonics **9**, 721 (2015).
20. S. Vasilyev, I. S. Moskalev, V. O. Smolski, J. M. Peppers, M. Mirov, A. V. Muraviev, K. Zawilski, P. G. Schunemann, S. B. Mirov, K. L. Vodopyanov, and V. P. Gapontsev, Optica **6**, 111 (2019).
21. T. P. Butler, D. Gerz, C. Hofer, J. Xu, C. Gaida, T. Heuermann, M. Gebhardt, L. Vamos, W. Schweinberger, J. A. Gessner, T. Siefke, M. Heusinger, U. Zeitner, A. Apolonski, N. Karpowicz, J. Limpert, F. Krausz, and I. Pupeza, Opt. Lett. **44**, 1730 (2019).
22. S. A. Diddams, J. Opt. Soc. Am. B **27**, B51 (2010).
23. I. Znakovskaya, E. Fill, N. Forget, P. Tournois, M. Seidel, O. Pronin, F. Krausz, and A. Apolonski, Opt. Lett **39**, 5471 (2014).
24. D. Sanchez, M. Hemmer, M. Baudisch, S. L. Cousin, K. Zawilski, P. Schunemann, O. Chalus, C. Simon-Boisson, and J. Biegert, Optica **3**, 147 (2016).
25. L. von Grafenstein, M. Bock, D. Ueberschaer, K. Zawilski, P. Schunemann, U. Griebner, and T. Elsaesser, Opt. Lett. **42**, 3796 (2017).
26. M. Hemmer, D. Sánchez, M. Jelínek, V. Smirnov, H. Jelinkova, V. Kubeček, and J. Biegert, Opt. Lett. **40**, 451 (2015).
27. L. von Grafenstein, M. Bock, D. Ueberschaer, U. Griebner, and T. Elsaesser, Opt. Lett. **41**, 4668 (2016).
28. K. T. Zawilski, P. G. Schunemann, S. D. Setzler, and T. M. Pollak, J. Cryst. Growth **310**, 1891 (2008).
29. H. Hoogland, A. Thai, D. Sanchez, S. L. Cousin, M. Hemmer, M. Engelbrecht, J. Biegert, and R. Holzwarth, Opt. Express **21**, 31390 (2013).
30. U. Elu, M. Baudisch, H. Pires, F. Tani, M. H. Frosz, F. Köttig, A. Ermolov, P. St.J. Russell, and J. Biegert, Optica **4**, 1024 (2017).
31. G. Arisholm, J. Opt. Soc. Am. B **14**, 2543 (1997).